photonics

MDPI

Article

Interference Generation of a Reverse Energy Flow with Varying Orbital and Spin Angular Momentum Density

Andrey V. Ustinov [1,*], Alexey P. Porfirev [1,2] and Svetlana N. Khonina [1,2]

[1] Image Processing Systems Institute, National Research Centre "Kurchatov Institute", Molodogvardeyskaya Str. 151, 443001 Samara, Russia; porfirev.alexey@ipsiras.ru (A.P.P.); khonina@ipsiras.ru (S.N.K.)
[2] Samara National Research University, Moskovskoye Shosse 34, 443086 Samara, Russia
* Correspondence: andr@ipsiras.ru

Abstract: This paper presents a novel method for generating and shaping reverse energy flow through the interference of light fields from a minimal number of point light sources. Until now, reverse energy flow has only been observed using complex light fields, such as optical vortices or cylindrical vector beams, limiting the formation of reverse energy flow near the optical axis. We demonstrate both analytically and numerically that unbounded regions of reverse energy flow can be achieved with just two point light sources, positioned asymmetrically at specific angles (e.g., 90 or 45 degrees) and with particular polarization states. The results indicate that the relative reverse energy flow can be enhanced by increasing the number of sources to three or four, adjusting their polarization, or introducing a vortex phase singularity. The presence of an initially embedded asymmetry in the fields under consideration leads to the formation of a non-uniform distribution of spin and orbital angular momentum density. Variations in the polarization state, as well as the introduction of a vortex phase singularity, allow for changing the distribution of angular momentum density while maintaining the presence of a reverse energy flow. We also explore the feasibility of implementing the obtained results using sectional phase diffractive optical elements, which will enhance the energy efficiency of the generated fields compared to point sources.

Keywords: energy flow; angular momentum; polarization; multi-beam interference; Richards–Wolf formulas

Citation: Ustinov, A.V.; Porfirev, A.P.; Khonina, S.N. Interference Generation of a Reverse Energy Flow with Varying Orbital and Spin Angular Momentum Density. *Photonics* **2024**, *11*, 962. https://doi.org/10.3390/photonics11100962

Received: 12 September 2024
Revised: 9 October 2024
Accepted: 10 October 2024
Published: 14 October 2024

1. Introduction

Great interest in the study of a wide variety of structured laser beams [1–7] is associated with various features of the characteristics of these optical fields, such as amplitude-phase distribution, polarization state, coherence, etc. Various properties of laser beams are in demand in various applications. For example, laser beams with a vortex phase singularity [8–12] are successfully used in optical tweezers and spanners [13–15], for multiplexing of optical data transmission channels [16–18], optical imaging and microscopy [19–21], as well as for laser processing and patterning of various materials [22–25]. Vector beams with inhomogeneous polarization are also used to solve the problem of overcoming the diffraction limit in optical microscopy, laser material processing, optical trapping and manipulation of nano- and microparticles, holography, and optical communications [26–35].

It should be noted that for various applications, a combination of both the phase and polarization distribution of the generated light field may be important. This makes it possible to control characteristics of the electromagnetic field, such as the energy flow and Poynting vector density [36–39], orbital and spin angular momentum (OAM and SAM) density [40–49], optical forces distribution [50–54], as well as their interrelation [55–63]. Thus, controlling the amplitude-phase and polarization state of the generated light field allows one to influence various characteristics of the field required in specific situations.

Currently, one of the primary methods for shaping structured vector beams involves the use of metasurfaces [64–67]. However, these devices are still complex and expensive

to manufacture for widespread use. A more common approach involves combining two orthogonally polarized light fields using diffractive optical elements (DOEs), spatial light modulators (SLMs), or digital micromirror devices (DMDs) [68–72]. Another method is the multi-beam interference of light fields with different polarization states from coherent sources [73–77]. In this scenario, various vector structured beams can be formed by adjusting the position of the sources and the polarization/focusing characteristics of the shaped light beams [78]. This method does not require the use of special optical elements but allows for dynamic control of the field's polarization structure.

We propose a simple method for shaping a reverse energy flow caused by the interference of light fields from a small number (two or three) of point light sources. Reverse energy flow refers to the direction of energy flow being opposite to the propagation direction of the beam [79]. This method can be utilized to move dielectric nanoparticles with absorption in the opposite direction to the laser beam's propagation, exerting a greater force compared to similar particles without absorption [80,81].

Previously, the potential for generating a reverse energy flow using circularly polarized optical vortex beams [82] and cylindrical vector beams [83–85] has been demonstrated. Typically, in these cases, the regions of the formation of the inverse energy flow are located near to the optical axis and are bounded (size is approximately of the order of the wavelength). To elongate the region of energy backflow, annular apertures [86,87] and specific phase or polarization distributions [88,89] have been suggested.

In this paper, we analytically and numerically demonstrate that unbounded regions of the reverse flow can be formed using only two point light sources located at equal distances from the origin of the coordinate system (see scheme in Figure 1). This is an important difference from the works [90,91], where interference patterns generated by four plane waves with linear polarization were considered. The magnitude of the reverse flow depends on both the angles between the radius vectors directed to the sources and on the polarization states of the sources. An important factor for the formation of the reverse flow is the asymmetric position of the two point sources, i.e., at an angle of 90 or 45 degrees between the radius vectors, depending on the polarization state. For two co-planar beams (located on the diameter of the circle), which were considered in the work [78], it is impossible to obtain a reverse energy flow.

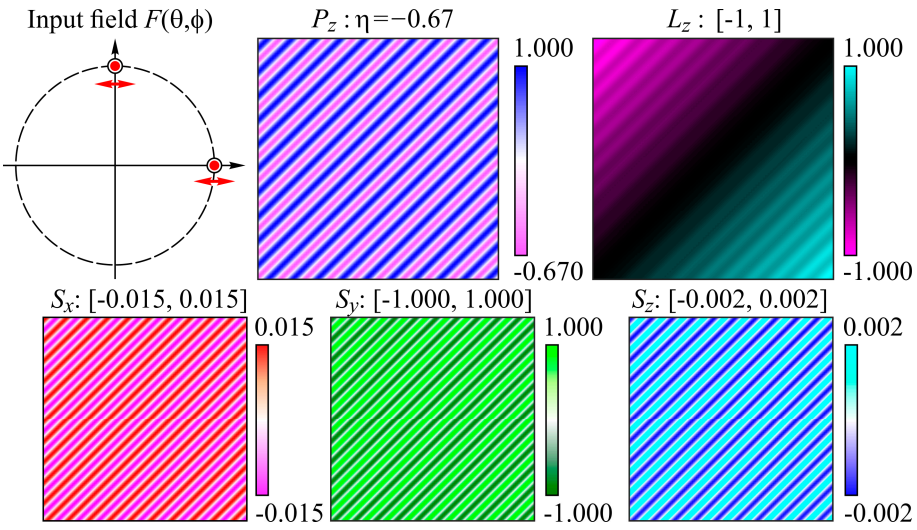

Figure 1. *Cont.*

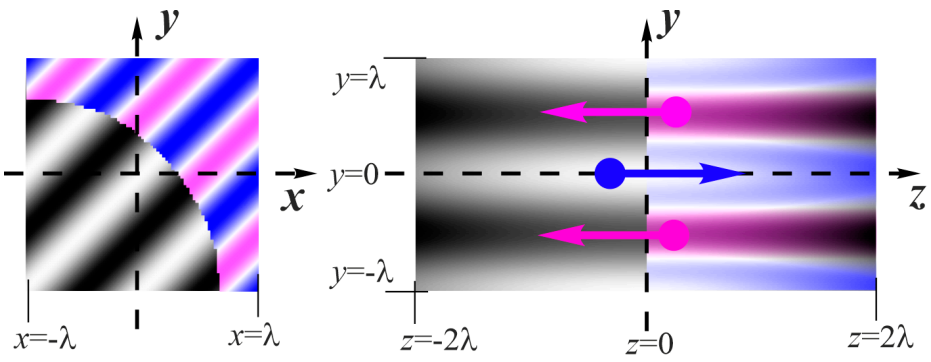

Figure 1. Results of numerical simulation for two point sources located in perpendicular directions with the same x-linear polarization. Top row: input field (**left**), longitudinal component of the Poynting vector P_z (blue for positive values, pink for negative) and longitudinal component of external OAM L_z (turquoise for positive values, pink for negative). Bottom row: components of the SAM density distribution (light shade corresponds to positive values, dark shade to negative). The bottom line shows the correspondence between the field intensity **E** and the distribution of P_z in the focal plane (**left**) and along the optical axis (**right**).

Thus, the light fields under investigation initially have a broken symmetry, which leads to the formation of a non-uniform angular momentum density [92]. Introducing a phase difference does not change the fact of the presence of a reverse energy flow, but can be used to vary the distribution of angular momentum. We also study the possibility of implementing the obtained results using sectional phase DOEs. This approach will enhance the energy efficiency of the generated fields in comparison to point sources.

2. Theoretical Background

There are various approaches to calculating the propagation and focusing of vector beams, for example, the method of expansion in plane waves [93,94] and vector Rayleigh–Sommerfeld integrals [95–97] convenient for calculating the field in the near diffraction zone [98]. In the far diffraction zone or focal region, Richards–Wolf formulas [99,100] are often used. Obviously, in all cases, the task of calculation and analysis is simplified if there is a possibility of obtaining an analytical solution [101,102]. In particular, in the works [103,104], an analysis of the formation of a reverse energy flow for vortex beams with different polarizations was performed based on the point complex source method [105,106]. However, in this paper, we consider solutions that are simple for experimental implementation (for example, a set of holes in a screen [78] or segments in an annular slit [86], supplemented by a lens), which are difficult to describe analytically. In this case, it is logical to use the Richards–Wolf formulas.

The components of the electric and magnetic field vectors in the case of tight focusing are calculated using the Richards–Wolf formulas [99]. In a spherical coordinate system, they are given by the expressions:

$$\begin{bmatrix}\mathbf{E}(r,\varphi,z)\\ \mathbf{H}(r,\varphi,z)\end{bmatrix} = -\frac{if}{\lambda}\int_0^{\Theta}\int_0^{2\pi} T(\theta)F(\theta,\phi)\begin{bmatrix}\mathbf{P}_E(\theta,\phi)\\ \mathbf{P}_H(\theta,\phi)\end{bmatrix}\exp[ik(r\sin\theta\cos(\phi-\varphi)+z\cos\theta)]\sin\theta d\theta d\phi \quad (1)$$

where

$$\begin{aligned}\mathbf{P}_E(\theta,\phi) &= \begin{bmatrix} A(\theta,\phi) & C(\theta,\phi)\\ C(\theta,\phi) & B(\theta,\phi)\\ -D(\theta,\phi) & -E(\theta,\phi)\end{bmatrix}\begin{pmatrix} c_x(\theta,\phi)\\ c_y(\theta,\phi)\end{pmatrix},\\ \mathbf{P}_H(\theta,\phi) &= \begin{bmatrix} C(\theta,\phi) & -A(\theta,\phi)\\ B(\theta,\phi) & -C(\theta,\phi)\\ -E(\theta,\phi) & D(\theta,\phi)\end{bmatrix}\begin{pmatrix} c_x(\theta,\phi)\\ c_y(\theta,\phi)\end{pmatrix},\end{aligned} \quad (2)$$

$$\begin{aligned} A(\theta,\phi) &= 1+\cos^2\phi(\cos\theta-1)\,,\\ B(\theta,\phi) &= 1+\sin^2\phi(\cos\theta-1)\,,\\ C(\theta,\phi) &= \sin\phi\cos\phi(\cos\theta-1)\,,\\ D(\theta,\phi) &= \cos\phi\sin\theta,\\ E(\theta,\phi) &= \sin\phi\sin\theta\,. \end{aligned} \tag{3}$$

In the above expressions (r, ϕ, z) are cylindrical coordinates in the focal region, (θ, ϕ) are spherical angular coordinates at the exit of the pupil of the focusing system, sin (Θ) = NA is the numerical aperture of the system, $F(\theta, \phi)$ is the transmission (input) function, $T(\theta)$ is the apodization function, $k = 2\pi/\lambda$ is the wave number, λ is the radiation wavelength, f is the focal length, and $\begin{pmatrix} c_x(\theta,\phi) \\ c_y(\theta,\phi) \end{pmatrix}$ is the polarization vector. We do not assume that it is standardized. For the focal plane, z is 0.

The longitudinal component of the Poynting vector (we do not calculate the transverse ones in this work, since they do not form a reverse flow) is defined by the formula:

$$P_z \,\mathrm{Re}\left[E_x H_y^* - E_y H_x^*\right] = \mathrm{Re}\left[E_x^* H_y - E_y^* H_x\right]. \tag{4}$$

Taking the real part in this expression corresponds to the classical definition. However, recent studies have revealed that the imaginary part of this component plays a role in the transverse force acting on optically trapped particles [107]. In most cases, the impact of the imaginary part is minimal compared to the real part [108,109]. Therefore, in this paper, we focus on the classical version represented by Equation (4).

The symmetry breaking in the beam structure leads to the formation of a non-uniform distribution of the angular momentum density. In particular, the SAM density distribution may be calculated by the following formula [110]:

$$\mathbf{S} = \begin{pmatrix} S_x \\ S_y \\ S_z \end{pmatrix} \simeq \mathrm{Im}\begin{pmatrix} E_y^* E_z - E_z^* E_y \\ E_z^* E_x - E_x^* E_z \\ E_x^* E_y - E_y^* E_x \end{pmatrix}. \tag{5}$$

Note that the longitudinal component of the SAM typically dominates and is associated with the presence of circular polarization in the generated field [111–113]. This allows trapped particles to rotate around their axis in the transverse plane. However, at sharp focusing, transverse components of the SAM may also exist [43,44,114,115], causing the particles to rotate around their axis in the direction of the light propagation. The coexistence of both transverse and longitudinal components [116] can result in the intricate 3D rotation of trapped particles.

Taking into account the spin–orbit interaction, we also consider the longitudinal component of the external OAM density distribution, associated with the breaking of the axisymmetric structure of the field [117,118]:

$$L_z \simeq \mathrm{Re}\left[x E_z^* E_x - y E_y^* E_z\right]. \tag{6}$$

Note that a non-zero value for expression (6) indicates a shift in the longitudinal component of the focused field, which, in turn, results in the emergence of the spin Hall effect of light [55,62,63,116,117].

3. Analytics and Numerical Illustrations for Two Point Sources

3.1. A Single Point Source

If we consider a single point source as $F(\theta, \phi)$ with the center at the point (θ_0, ϕ_0), radial dimension $\Delta\theta$ and angular dimension $\Delta\phi$, then based on Equations (1) and (2) at

$z = 0$ (in the focal plane), we can write approximate expressions (the factor in front of the integral is omitted):

$$\begin{array}{l} E_x^* \; R\Delta\phi \exp(-ikr\sin\theta_0\cos(\phi_0-\varphi)) \times \Big[A(\phi_0)c_x^*(\phi_0) + C(\phi_0)c_y^*(\phi_0)\Big], \\ E_y^* \; R\Delta\phi \exp(-ikr\sin\theta_0\cos(\phi_0-\varphi)) \times \Big[C(\phi_0)c_x^*(\phi_0) + B(\phi_0)c_y^*(\phi_0)\Big], \\ H_x \; R\Delta\phi \exp(+ikr\sin\theta_0\cos(\phi_0-\varphi)) \times \big[C(\phi_0)c_x(\phi_0) - A(\phi_0)c_y(\phi_0)\big], \\ H_y \; R\Delta\phi \exp(+ikr\sin\theta_0\cos(\phi_0-\varphi)) \times \big[B(\phi_0)c_x(\phi_0) - C(\phi_0)c_y(\phi_0)\big], \end{array} \tag{7}$$

where $R = \Delta\theta T(\theta_0)\sin\theta_0$.

If we substitute the components of the fields defined by Equation (7) into Equation (4) and take into account Equation (3), we obtain

$$P_z = (R\Delta\phi)^2 \cos\theta_0 \Big(|c_x(\phi_0)|^2 + |c_y(\phi_0)|^2\Big). \tag{8}$$

This is a positive value, which means that there can be no reverse energy flow with a single point source. In addition, the value in Equation (8) does not depend on r and φ, i.e., it is the same across the entire focal plane.

3.2. Two Point Sources

With two or more sources, Equation (7) remains true for each of them separately (taking into account their parameters), and the total electric and magnetic fields will be equal to their sum. To simplify the expressions, we will assume that $\Delta\theta$ and $\Delta\phi$ are the same for all sources, and that they themselves are located on one ring with a radius θ_0. In this case, the multiplier $R\Delta\phi$ will be the same for all fields and will not be written down in the following expressions. Exponential factors for two sources will no longer be reduced, and a dependence on r and φ will appear. The right side of Equation (4) after the transformations will be equal to

$$\begin{array}{l} E_x^* H_y - E_y^* H_x = \Big(|c_{x1}|^2 + |c_{y1}|^2 + |c_{x2}|^2 + |c_{y2}|^2\Big)\cos\theta_0 + \\ + e^{ip\alpha}\big[(B_1A_2 - C_1C_2)c_{x1}c_{x2}^* + (B_1C_2 - C_1B_2)c_{x1}c_{y2}^* - \\ - (C_1A_2 - A_1C_2)c_{y1}c_{x2}^* - (C_1C_2 - A_1B_2)c_{y1}c_{y2}^*\Big] + \\ + e^{-ip\alpha}\big[(A_1B_2 - C_1C_2)c_{x1}^*c_{x2} - (A_1C_2 - C_1A_2)c_{x1}^*c_{y2} + \\ + (C_1B_2 - B_1C_2)c_{y1}^*c_{x2} - (C_1C_2 - B_1A_2)c_{y1}^*c_{y2}\big] \end{array} \tag{9}$$

where $p = kr\sin\theta_0$; $\alpha = \cos(\phi_1 - \varphi) - \cos(\phi_2 - \varphi)$. If the quantities $c_x(\phi)$ and $c_y(\phi)$ are real, then the procedure for taking the real part is simplified, and as a result we obtain the following expression for P_z:

$$\begin{array}{l} P_z = \Big(c_{x1}^2 + c_{y1}^2 + c_{x2}^2 + c_{y2}^2\Big)\cos\theta_0 + \\ + \cos p\alpha\big[(A_1B_2 + B_1A_2 - 2C_1C_2)\big(c_{x1}c_{x2} + c_{y1}c_{y2}\big) + \\ + (C_2(A_1 - B_1) + C_1(B_2 - A_2))\big(c_{y1}c_{x2} - c_{x1}c_{y2}\big)\big] \end{array} \tag{10}$$

In its explicit form it looks like

$$\begin{array}{l} P_z = \Big(c_{x1}^2 + c_{y1}^2 + c_{x2}^2 + c_{y2}^2\Big)\cos\theta_0 + \\ + \cos\Big[2kr\sin\theta_0 \cdot \sin\frac{\phi_1-\phi_2}{2}\sin\Big(\frac{\phi_1+\phi_2}{2} - \varphi\Big)\Big] \times \\ \times\Big[\big(c_{x1}c_{x2} + c_{y1}c_{y2}\big)\Big(2\cos\theta_0 + (1-\cos\theta_0)^2\sin^2(\phi_1 - \phi_2)\Big) + \\ + 0.5\,\big(c_{y1}c_{x2} - c_{x1}c_{y2}\big)(1-\cos\theta_0)^2\sin 2(\phi_1 - \phi_2)\Big]. \end{array} \tag{11}$$

Even after assuming that the polarization coefficients are real numbers, Equation (11) still remains quite complex. Therefore, below we will consider some specific cases where simplifications are possible.

3.3. Proportional Relationships of Polarization Coefficients

One of the simplifications of Equation (10) is provided under the condition (we assume $c_{x1} \neq 0$):

$$c_{y1}c_{x2} - c_{x1}c_{y2} = 0 \;\Leftrightarrow\; c_{y2} = \frac{c_{y1}c_{x2}}{c_{x1}}. \tag{12}$$

Since the determinant of the components of the polarization vectors is zero, this condition corresponds to proportional relationships of the polarization coefficients. In this case, instead of Equation (11), we obtain

$$\begin{aligned} P_z = &\left(c_{x1}^2 + c_{y1}^2 + c_{x2}^2\left(1 + c_{y1}^2/c_{x1}^2\right)\right)\cos\theta_0 + \\ &+ \cos\left[2kr\sin\theta_0 \sin\tfrac{\phi_1-\phi_2}{2}\sin\left(\tfrac{\phi_1+\phi_2}{2} - \varphi\right)\right]\times \\ &\times\left(c_{x1}c_{x2} + c_{y1}^2 c_{x2}/c_{x1}\right)\left[2\cos\theta_0 + (1-\cos\theta_0)^2\sin^2(\phi_1-\phi_2)\right] \end{aligned} \tag{13}$$

For convenience, we introduce the following notations:

$$\begin{aligned} &U(\phi_1,\phi_2,\varphi) = \cos\left[2kr\sin\theta_0\sin\tfrac{\phi_1-\phi_2}{2}\sin\left(\tfrac{\phi_1+\phi_2}{2} - \varphi\right)\right], \\ &Q_1(\phi_1,\phi_2) = 2\cos\theta_0 + (1-\cos\theta_0)^2\sin^2(\phi_1-\phi_2). \end{aligned} \tag{14}$$

Note that the value $Q_1(\phi_1,\phi_2)$ is always positive.

Let us rewrite Equation (13) as follows:

$$P_z = \left(c_{x1}^2 + c_{y1}^2 + c_{x2}^2\left(1 + \frac{c_{y1}^2}{c_{x1}^2}\right)\right)\cos\theta_0 + U(\phi_1,\phi_2,\varphi)Q_1(\phi_1,\phi_2)\left(c_{x1}c_{x2} + c_{y1}^2\frac{c_{x2}}{c_{x1}}\right). \tag{15}$$

If c_{x1}, c_{x2}, c_{y1} are positive, then c_{y2} is also positive. The extrema of Equation (15) will be at $\phi_2 - \phi_1 = 90^\circ$ (the sources are located in perpendicular directions) and $U(\phi_1,\phi_2,\varphi) = \pm 1$. In explicit form:

$$(P_z)_{\substack{\max\\\min}} = \left(c_{x1}^2 + c_{y1}^2 + c_{x2}^2\left(1 + \frac{c_{y1}^2}{c_{x1}^2}\right)\right)\cos\theta_0 \pm \left(c_{x1}c_{x2} + c_{y1}^2\frac{c_{x2}}{c_{x1}}\right)(1+\cos^2\theta_0). \tag{16}$$

Note that with sharp focusing, i.e., when $\cos\theta_0 \xrightarrow[\theta_0\to 90^\circ]{} 0$, the minimum of this expression is negative, which corresponds to the appearance of a reverse energy flow.

Usually, when describing the phenomenon of reverse flow, an important characteristic is not only its magnitude but also its ratio to the largest possible value of the forward flow [84,86].

If we introduce the notation $q_1 = \frac{c_{x1}c_{x2} + c_{y1}^2 c_{x2}/c_{x1}}{c_{x1}^2 + c_{y1}^2 + c_{x2}^2\left(1 + c_{y1}^2/c_{x1}^2\right)}$, then the ratio of the minimum value of the energy flow to the maximum value will be equal to:

$$\eta = \frac{(P_z)_{\min}}{(P_z)_{\max}} = \frac{\cos\theta_0 - q_1(1-\cos\theta_0)^2}{\cos\theta_0 + q_1(1-\cos\theta_0)^2}. \tag{17}$$

As can be seen from Equation (17), at $\theta_0 = 90^\circ$, the minimum negative relative value $\eta = -1$ (the greatest presence of reverse energy flow) is achieved regardless of q_1. If some value θ_0 is defined, then the minimum of the ratio η will be at the maximum achievable

value of q_1 (the derivative with respect to q is negative). It can be shown that the maximum value $q_1 = 0.5$ is achieved at $c_{x1}/c_{x2} = 1$ (regardless of c_{y1}). Then, the ratio will be equal to:

$$\eta = -\frac{(1-\cos\theta_0)^2}{(1+\cos\theta_0)^2}. \tag{18}$$

Thus, the best results are achieved with equal $c_{x2} = c_{x1}$ and arbitrary c_{y1}. However, taking into account Equation (12), we obtain that $c_{y2} = c_{y1}c_{x2}/c_{x1} = c_{y1}$.

This means that for two point sources with the same polarization, located in perpendicular directions ($\phi_2 - \phi_1 = 90°$), there is always a reverse energy flow. Its relative magnitude increases with increasing angle θ_0 (i.e., focusing sharpness) and reaches an extremum of $\eta = -1$ at $\theta_0 = 90°$.

Although there are studies in which the ratio η reached higher values ($|\eta| \geq 1$) [83,84], the regions of the reverse flow in these cases had either a finite area or an infinite area, but of measure zero with respect to the entire focal plane [86,88,89]. In the case under consideration, the interference generation method provides theoretically infinite regions of the reverse flow, the fraction of which is close to half of the total focal plane. A similar situation was described in works [90,91], where the interference of four plane waves was considered and limited rectangular regions of the reverse flow were formed. The fraction of these regions was approximately half of the focal region. In this work, the difference lies not only in the exhaustive analysis of the conditions for achieving the reverse flow during the interference of fields formed by several point sources (taking into account their positions and polarization states), but also the possibility of forming unlimited strip regions of the reverse flow.

Figures 1 and 2 display the results of numerical modeling for two point sources located in perpendicular directions with the same polarization. For linear polarization (Figure 1), we also showed (bottom row) a visual correspondence between the **E** field intensity and the distribution of P_z in the focal plane (left) and along the optical axis (right). It is seen that the regions of negative values of P_z coincide with the regions of minimal values of the **E** field intensity.

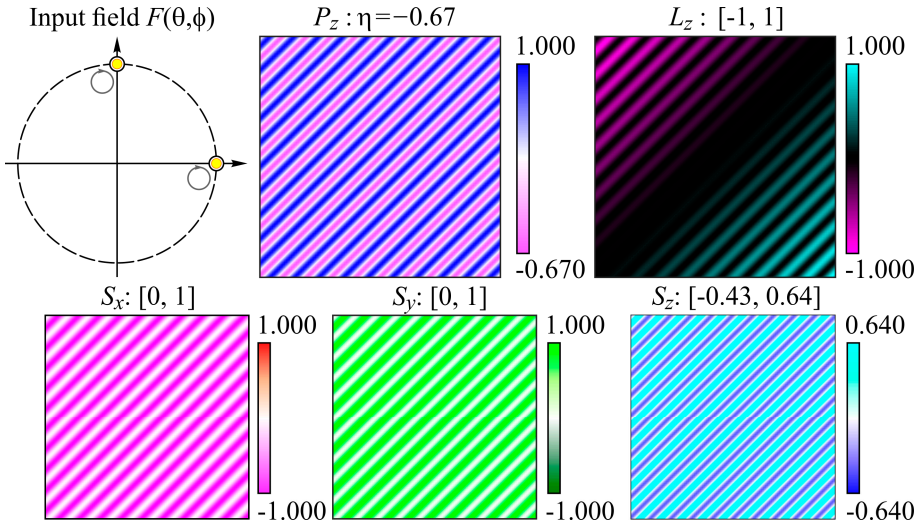

Figure 2. Results of numerical simulation for two point sources located in perpendicular directions with the same circular polarization. The labels and colors correspond to the labels and colors in Figure 1.

Strictly speaking, circular polarization (Figure 2) is not covered in the analytical discussion provided in this section, as one of the polarization coefficients is imaginary. However, as depicted in Figure 2, in this scenario, there is also a reverse energy flow, nearly equivalent to that achieved with linear polarization.

The results were obtained using Equations (1)–(6) with the following parameters: wavelength is λ = 1 μm, input field size is 200 μm × 200 μm, the output field size is 10 μm × 10 μm, numerical aperture NA = 0.99. Point sources in the calculations had a radius equal to the wavelength λ.

As can be seen, the distribution of all quantities in both cases is one-dimensional, i.e., it represents stripes located at an angle of 45° (=90°/2). This is quite expected based on the geometry of the location of two point sources.

Comparison of Figures 1 and 2 shows that the energy flux distribution pattern P_z and the η ratio are the same, although the polarization type in the sources changes. This change has a minor effect on the OAM distribution pattern and a much more significant effect on the SAM distribution. For linear polarization (Figure 1), the averaged values in each component are zero, while for circular polarization (Figure 2), they have a positive value (this is also expected, since the right-handed, i.e., "positive", circular polarization is considered).

Note that for $\phi_2 - \phi_1 = 180°$ (co-planarly located sources) the value P_z will always be non-negative. For such an arrangement, it is equal to $P_z = \cos\theta_0(c_{x1}^2 + c_{x2}^2 + 2\cos(2kr\sin\theta_0\cos(\varphi - \phi_2))c_{x1}c_{x2})$; and this expression is non-negative, since the coefficient for $c_{x1}c_{x2}$ is no greater than two in modulus. Various field characteristics obtained during the interference of co-planarly located sources with different polarization states were examined in detail in [78].

3.4. Orthogonal States of Polarization

Another option for simplifying Equation (10) arises when both c_x and c_y are nonzero and the equality holds:

$$c_{x1}c_{x2} + c_{y1}c_{y2} = 0 \;\Leftrightarrow\; c_{y2} = -\frac{c_{x1}c_{x2}}{c_{y1}}. \tag{19}$$

Equation (19) corresponds to orthogonal polarization states. In this case, instead of Equation (13), we obtain:

$$\begin{aligned} P_z = &\left(c_{x1}^2 + c_{y1}^2 + c_{x2}^2\left(1 + \tfrac{c_{x1}^2}{c_{y1}^2}\right)\right)\cos\theta_0 + \\ &+ \cos\left[2kr\sin\theta_0\sin\tfrac{\phi_1-\phi_2}{2}\sin\left(\tfrac{\phi_1+\phi_2}{2} - \varphi\right)\right]\times \\ &\times\tfrac{1}{2}\left(c_{y1}c_{x2} + c_{x1}^2\tfrac{c_{x2}}{c_{y1}}\right)(1-\cos\theta_0)^2\sin 2(\phi_2 - \phi_1) \end{aligned} \tag{20}$$

Taking into account Equation (14) and introducing the notation

$$Q_2(\phi_1, \phi_2) = 0.5(1 - \cos\theta_0)^2\sin 2(\phi_2 - \phi_1), \tag{21}$$

let us rewrite Equation (20) as follows:

$$P_z = \left[c_{x1}^2 + c_{y1}^2 + c_{x2}^2\left(1 + \frac{c_{x1}^2}{c_{y1}^2}\right)\right]\cos\theta_0 + U(\phi_1, \phi_2, \varphi)Q_2(\phi_1, \phi_2)\left(c_{y1}c_{x2} + c_{x1}^2\frac{c_{x2}}{c_{y1}}\right) \tag{22}$$

The bracket in the second term of Equation (22) is positive. The maximum of P_z will be when $U(\phi_1, \phi_2, \varphi) = 1$, and $Q_2(\phi_1, \phi_2)$ reaches its maximum value, that is, when $\phi_2 - \phi_1 = 45°$ (the maximum is equal to $0.5(1 - \cos\theta_0)^2$). Substituting into Equation (22) gives

$$(P_z)_{\max} = \left[c_{x1}^2 + c_{y1}^2 + c_{x2}^2\left(1 + \frac{c_{x1}^2}{c_{y1}^2}\right)\right]\cos\theta_0 + \frac{1}{2}(1 - \cos\theta_0)^2\left(c_{y1}c_{x2} + c_{x1}^2\frac{c_{x2}}{c_{y1}}\right). \tag{23}$$

Similarly, the minimum of P_z will be when $Q_2(\phi_1, \phi_2)$ is still maximum, and $U(\phi_1, \phi_2, \varphi) = -1$. This minimum is equal to

$$(P_z)_{\min} = \left[c_{x1}^2 + c_{y1}^2 + c_{x2}^2\left(1 + \frac{c_{x1}^2}{c_{y1}^2}\right)\right]\cos\theta_0 - \frac{1}{2}(1-\cos\theta_0)^2\left(c_{y1}c_{x2} + c_{x1}^2\frac{c_{x2}}{c_{y1}}\right). \quad (24)$$

From Equation (24), it follows that the minimum will be negative only in the non-paraxial case, when $\cos\theta_0 \xrightarrow[\theta_0 \to 90^\circ]{} 0$.

In the general case, the expression for determining the exact boundary θ_0 required to form a reverse flow is cumbersome, so we will give it only for the case $c_{x1} = 0$:

$$\cos\theta_0 < \frac{2\left(c_{y1}^2 + c_{x2}^2 + c_{y1}c_{x2}\right) - 2\sqrt{c_{y1}^2 + c_{x2}^2}(c_{y1} + c_{x2})}{2c_{y1}c_{x2}}. \quad (25)$$

The ratio of the minimum value to the maximum value is as follows:

$$\eta = \frac{(P_z)_{\min}}{(P_z)_{\max}} = \frac{\cos\theta_0 - q_2(1-\cos\theta_0)^2}{\cos\theta_0 + q_2(1-\cos\theta_0)^2}, \quad (26)$$

where $q_2 = \frac{1}{2}\frac{c_{y1}c_{x2} + c_{x1}^2 c_{x2}/c_{y1}}{c_{x1}^2 + c_{y1}^2 + c_{x2}^2\left(1 + c_{x1}^2/c_{y1}^2\right)}$.

Similar to the case considered in the previous section, at $\theta_0 = 90^\circ$, the minimum negative relative value $\eta = -1$ (the greatest presence of reverse energy flow) is achieved, regardless of q_2. If some value θ_0 is defined, then the minimum of the ratio η will be at the maximum achievable value $q_2 = 0.5$ (at $c_{y1}/c_{x2} = 1$, regardless of c_{x1}). Then, instead of Equation (26), we obtain the following expression:

$$\eta = -\frac{(1-\cos\theta_0)^2 - 4\cos\theta_0}{(1+\cos\theta_0)^2}. \quad (27)$$

The relation defined by Equation (27) is not so good as in Equation (18). Moreover, if $\cos\theta_0 > 3 - 2\sqrt{2}$ $(\theta_0 < 80^\circ 7')$, then the minimum will be positive, so that the reverse flow is present only when focusing at large angles $(\theta_0 > 80^\circ 7')$.

Thus, for two point sources with orthogonal polarization, a reverse energy flow is formed if they are located in directions at 45 degrees $(\phi_2 - \phi_1 = 45^\circ)$ and there is a sharp focusing $(\theta_0 > 80^\circ 7')$. The relative magnitude of the reverse flow reaches an extremum $\eta = -1$ at $\theta_0 = 90^\circ$. Note that this analysis is valid only for real polarization coefficients, i.e., it is not applicable to elliptical polarization.

Figures 3 and 4 show the results of numerical simulation for two point sources with orthogonal polarization states. The angle between the sources is 45 degrees. The theoretical considerations provided in this section align with the results depicted in Figure 3.

In this case, the distribution of all values also takes the form of stripes located at an angle of 22.5° (=45°/2). Since both cases actually exhibit linear polarization (although in Figure 4 it is non-uniform), the distributions of the SAM density projections have a mean equal to zero. The value of η for Figure 3 is worse than for Figure 1, which corresponds to the given Equations (18) and (27).

Although the relative values of the reverse flux η in this situation are worse than those obtained in the previous paragraph (as theoretically predicted in Equations (18) and (27)), the combination of the locations of several point sources, considering both configurations, can be utilized for various variations of the generated interference fields.

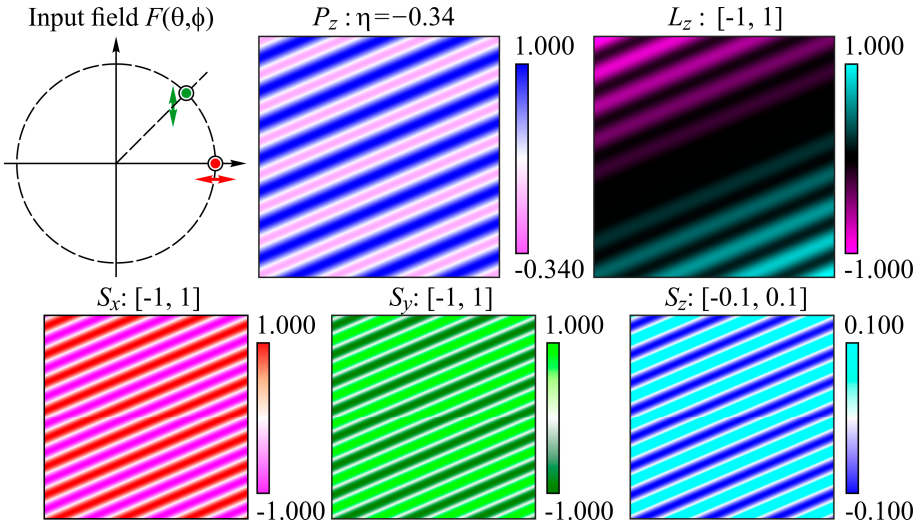

Figure 3. Results of numerical simulation for two point sources with orthogonal linear polarizations. The angle between the sources is 45 degrees. The labels and colors correspond to the labels and colors in Figure 1.

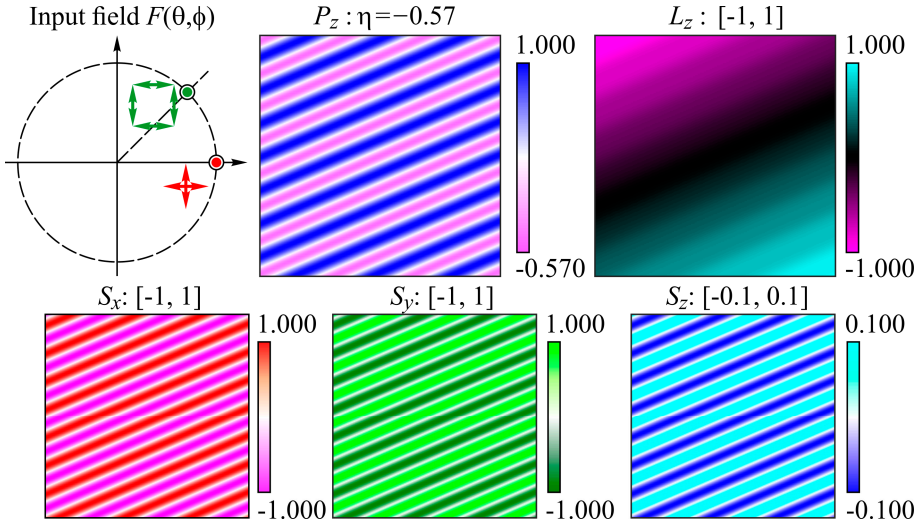

Figure 4. Results of numerical simulation for two point sources with orthogonal cylindrical polarizations (radial and azimuthal). The angle between the sources is 45 degrees. The labels and colors correspond to the labels and colors in Figure 1.

4. Interference Formation of Reverse Flow in Different Configurations of Point Light Sources

From the results presented above, it follows that by arranging the point light sources and choosing their polarization states, it is possible not only to form regions with a reverse energy flow but also to vary the density of the angular momentum distribution. An additional degree of freedom is the combination of the two configurations considered above.

4.1. Three Point Light Sources

Figures 5–7 show the results of numerical modeling for the case of three point sources with orthogonal polarization states. The angles between the sources are 45 degrees. The results reveal a significant increase in the complexity of the distribution structures being analyzed. The areas of reverse flow become segregated, with the exception of the circular polarization case (Figure 6).

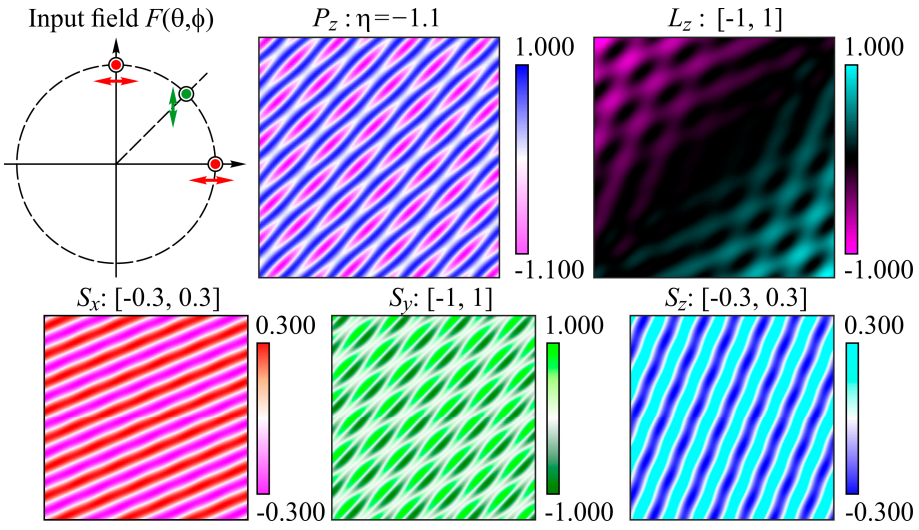

Figure 5. Results of numerical simulation for three point sources with orthogonal linear polarizations. The labels and colors correspond to the labels and colors in Figure 1.

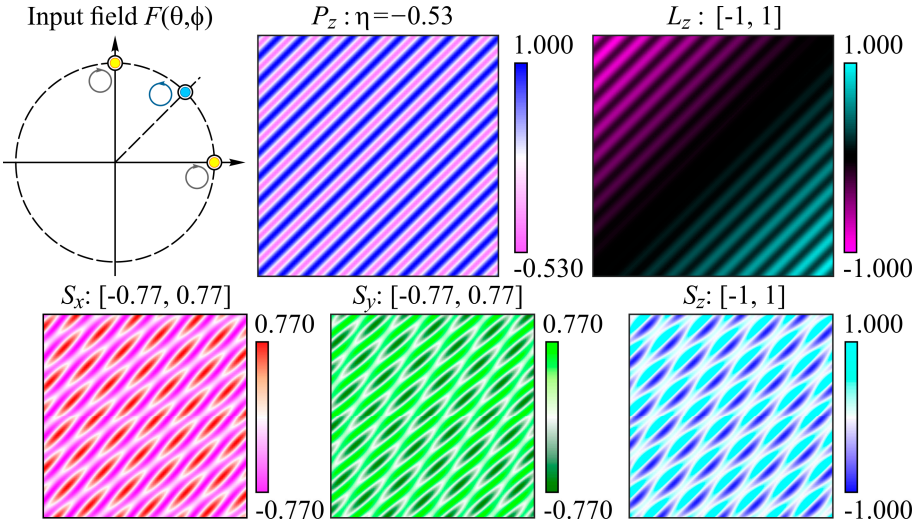

Figure 6. Results of numerical simulation for three point sources with orthogonal circular polarizations. The labels and colors correspond to the labels and colors in Figure 1.

The case shown in Figure 5 is interesting because the relative magnitude of the reverse flow η increased significantly. We can assume that there is one pair of point sources with an angle of 90 degrees between them and two sources with an angle of 45 degrees. Due to this, the value of η is better than for the previously considered cases, although it is smaller in absolute value than the algebraic sum of η from each pair. Even more important is that the stripes in the pictures are not strictly straight, which also affected the distribution of OAM and SAM density. At the same time, S_x retained a striped structure at an angle of 22.5°, and S_z at an angle of 67.5°. Note that the areas with negative values P_z are closed.

Using three point sources with orthogonal circular polarizations impaired the value of the relative return flux η compared to two identical polarizations. This is most likely explained by the fact that a pair of points with opposite circular polarization with an angle of 45 degrees between the points does not give a reverse flux and, therefore, adding a third point impaired the result. The stripes in the distributions of P_z and L_z remained straight, while all the components of the SAM became more complex in structure. Note that the transverse components S_x and S_y have large areas with positive values, while in the case of S_z the average value is zero.

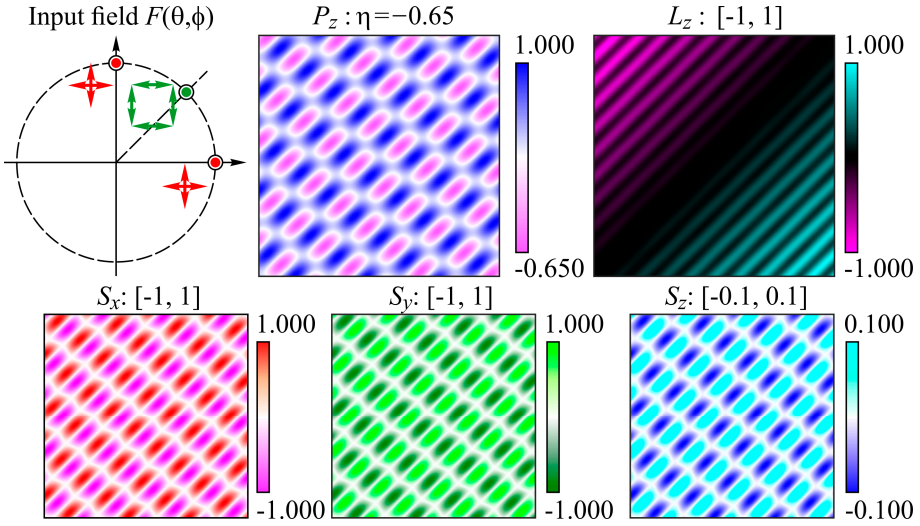

Figure 7. Results of numerical simulation for three point sources with orthogonal cylindrical polarizations. The labels and colors correspond to the labels and colors in Figure 1.

The results for the relative reverse flux η in Figure 7 are better than those in Figure 4 for the two orthogonal polarizations, but not by much. The distribution for P_z and SAM has a mosaic structure, while the OAM density pattern retains straight lines. The average values of all SAM components are zero.

Note that it is possible to extend the considered configurations to other quadrants (see Figure 8). This extension also alters the interference structure, but the presence of the reverse flow η remains in roughly the same proportion as for the three sources.

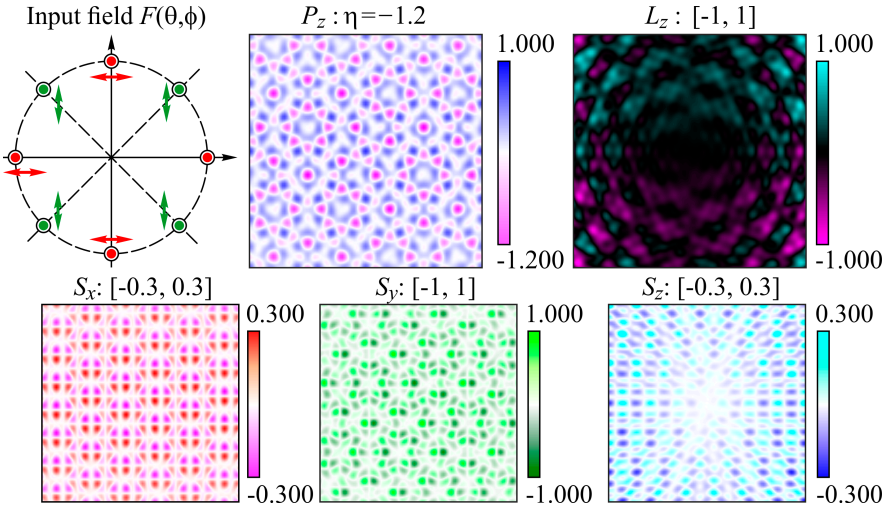

Figure 8. Results of numerical simulation for 8 point sources with orthogonal linear polarizations. The labels and colors correspond to the labels and colors in Figure 1.

Point light sources provide a low level of energy. Therefore, in the next section, we will discuss alternating orthogonal polarization states for non-point sources.

4.2. Segmented Annular-Shaped Polarization-Phase Elements

In this section, we consider ring segments instead of point sources, which can reduce the relative magnitude of the reverse energy flow but increase the total amount of energy entering the focal region. In this case, we use orthogonal polarization states similar to the previous section with continuation to other quadrants. As can be seen from the results shown in Figures 9–11, the presence of the reverse energy flow is preserved everywhere,

although its relative magnitude η decreased in absolute value, which is associated with the increase in point regions to ring segments.

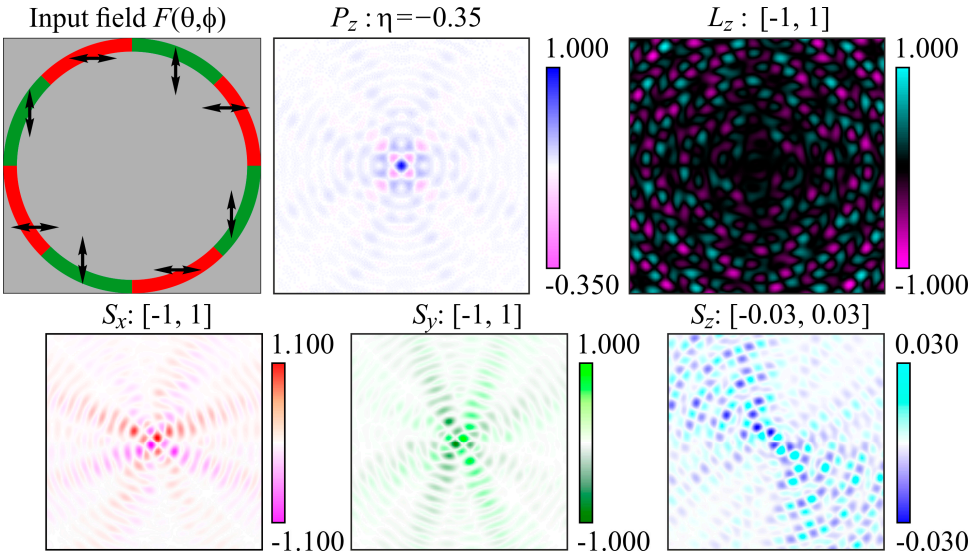

Figure 9. Results of numerical simulation for a segmented ring distribution with orthogonal linear polarizations. The labels and colors correspond to the labels and colors in Figure 1.

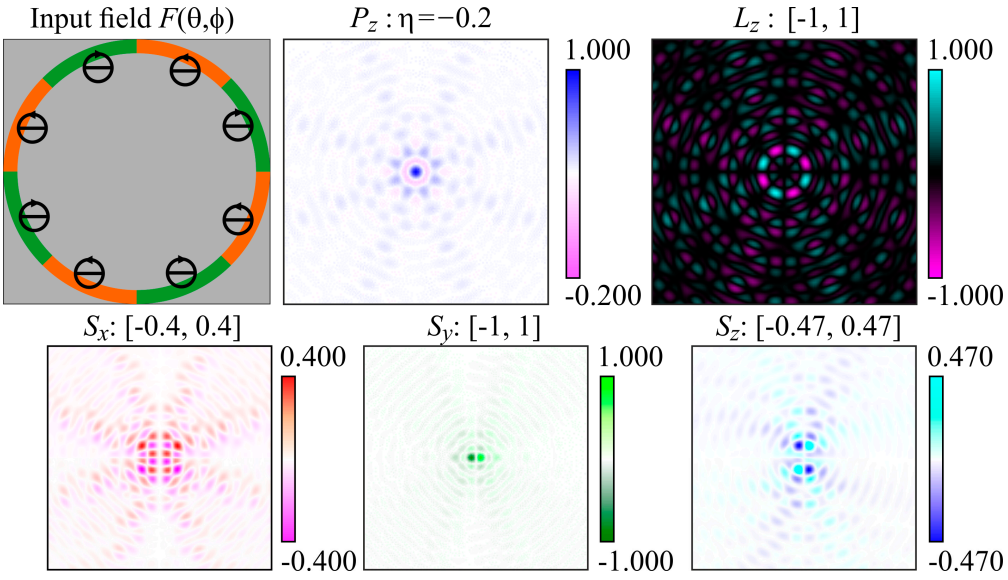

Figure 10. Results of numerical simulation for a segmented ring distribution with orthogonal circular polarizations. The labels and colors correspond to the labels and colors in Figure 1.

For orthogonal linear polarizations (Figure 9), the distribution pattern of P_z has a rotational symmetry of the 4th order. The OAM and SAM density distributions are noticeably less symmetrical and have zero values on average. For orthogonal circular polarizations (Figure 10), the distribution patterns P_z and L_z have a rotational symmetry of the 8th order. Moreover, there is a ring of negative values of P_z in the central part.

When using orthogonal cylindrical polarizations (Figure 11), in contrast to previous cases, a rather high value of η is observed. This observation likely correlates with previously obtained results on the presence of a reverse flow for beams with radial and azimuthal polarizations with orders greater than one [84,85].

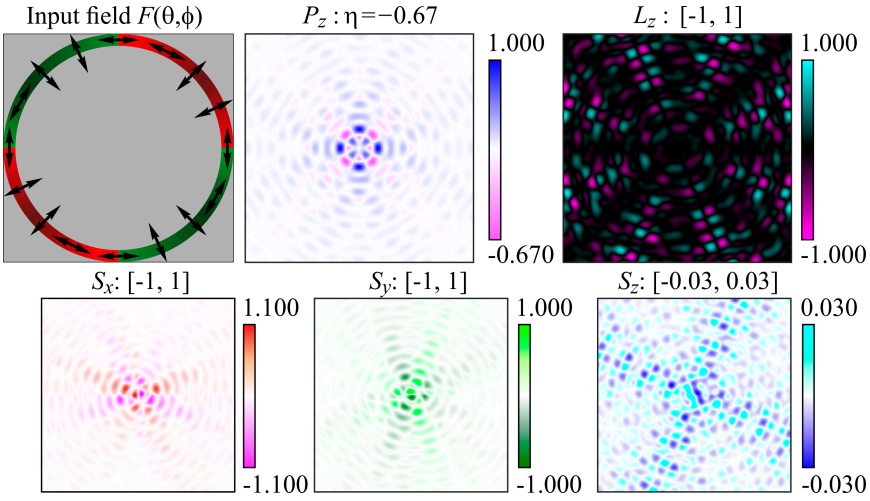

Figure 11. Results of numerical simulation for a segmented annular distribution with orthogonal cylindrical polarizations (radial and azimuthal). The labels and colors correspond to the labels and colors in Figure 1.

As can be seen from the examples provided, when a ring structure is used, the distribution of P_z can be noticeably altered by changing the polarization type. However the SAM and OAM density distributions do not change qualitatively. Nevertheless, the distribution of OAM density can be significantly changed by adding a spiral phase plate (SPP) [119]. The complex transmission function of the SPP is described by the phase function $\exp(im\varphi)$, where m is the order of the vortex phase singularity. Consequently, the energy flow structure should also undergo changes [88]. The corresponding calculation results are presented in Figures 12–14.

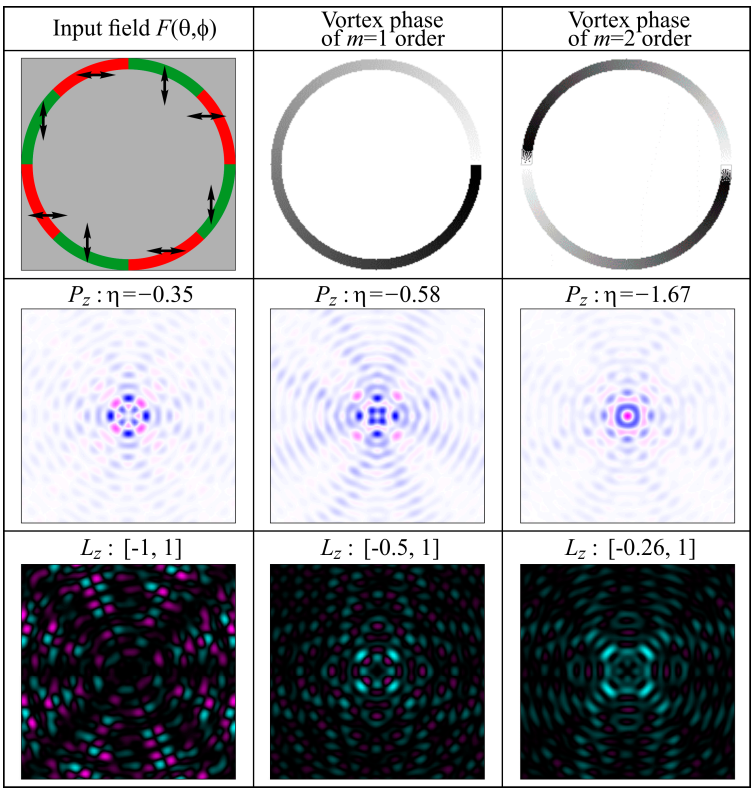

Figure 12. Results of numerical simulation for a segmented annular distribution with orthogonal linear polarizations with the introduction of a vortex phase singularity of the m-th order (in the left column for comparison m = 0).

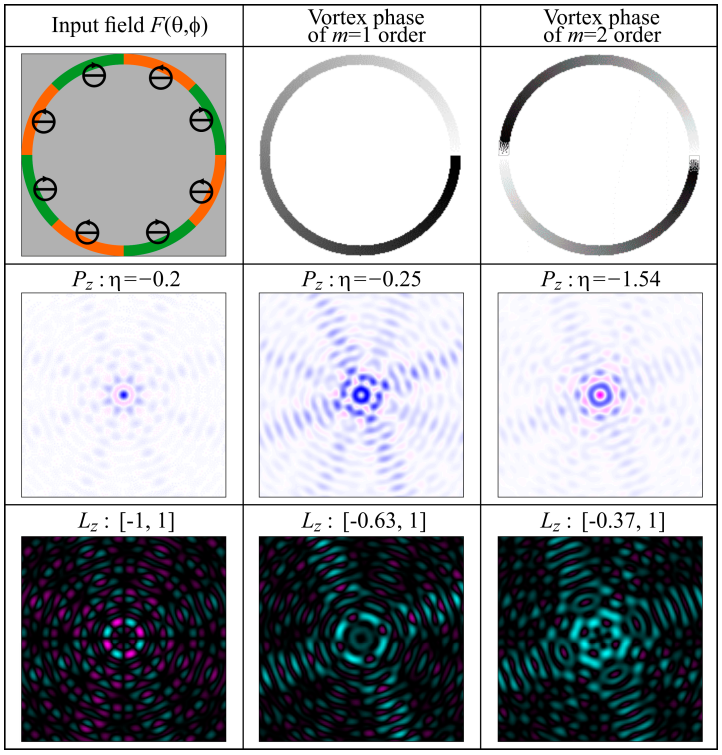

Figure 13. Results of numerical simulation for a segmented annular distribution with orthogonal circular polarizations with the introduction of a vortex phase singularity of the m-th order (in the left column for comparison m = 0).

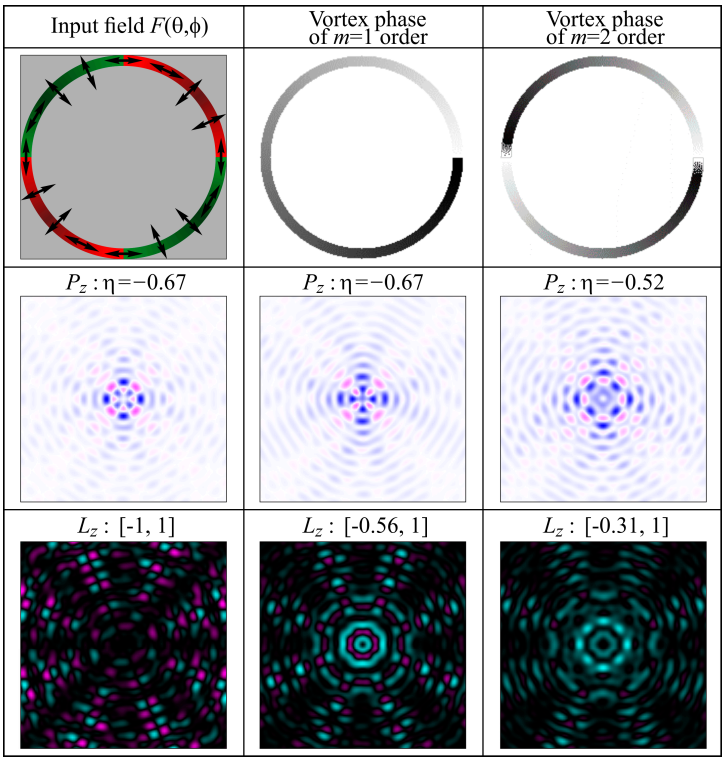

Figure 14. Results of numerical simulation for a segmented annular distribution with orthogonal cylindrical polarizations with the introduction of a vortex phase singularity of the m-th order (in the left column for comparison m = 0).

As can be seen, the most noticeable consequence of introducing a positive charge vortex phase was a change in the OAM density distribution; at m = 0 (left columns), an equal number of positive and negative values is observed, which leads to a zero average OAM, but in the presence of a vortex phase m = 1 (middle column), the clear majority of values became positive, and at a higher charge m = 2 (right column), the number and relative magnitude of positive values also increases.

However, a more interesting effect of introducing a vortex phase singularity is the enhancement of the relative reverse energy flux η for linear and circular polarization types (Figures 12 and 13), especially in the case of m = 2. Maximization of the relative reverse flux for a second-order vortex phase was previously observed for uniform circular [83] and linear [86] polarization. Such maximization is achieved by concentrating the reverse energy flux at the central point of the focal plane (on the optical axis). A demonstration of a similar effect for alternating orthogonal polarization states is shown in this work for the first time. For orthogonal cylindrical polarizations (Figure 14), introducing a vortex phase singularity leads to a shift of regions with negative values of P_z from the center to the periphery, which affects a decrease in the absolute value of η.

5. Discussion

In Section 3, it is analytically shown that the greatest relative value of the reverse flow is obtained when two points are located with a longitude difference of 90 degrees and the same linear polarization at these points. The question arises: Is it possible to improve the result by adding points? Since it has already been proven that the linear polarization can be arbitrary, and it is the difference in the directions of the points that is important, then, taking into account the form of Equations (1)–(4) and (7), for the sake of simplifying the calculations, we will place 4 points in positions with directions of 0, 90, 180, and 270 degrees, respectively. The polarization vector at all points will be taken equal to the linear x-polarization. Calculations according to Equation (7) yield the following values of the field components:

$$\begin{array}{l} E_y^* = H_x = 0 \;\; for\, all\, dots; \\ D1: E_x^* = e^{-ipx}\cos\theta_0, \;\; H_y = e^{ipx}; \\ D2: E_x^* = e^{-ipy}, \;\; H_y = e^{ipy}\cos\theta_0; \\ D3: E_x^* = e^{ipx}\cos\theta_0, \;\; H_y = e^{-ipx}; \\ D4: E_x^* = e^{ipy}, \;\; H_y = e^{-ipy}\cos\theta_0; \\ where \;\; p = k\sin\theta_0. \end{array} \quad (28)$$

5.1. Two Sources

The main results are in Section 3.1, but for ease of analysis, we will write down all the expressions here. For a pair of points ($D1$, $D3$) and for a pair of points ($D2$, $D4$), the difference in directions is 180 degrees, and the energy flow values will only be non-negative, as mentioned above. For pairs ($D1$, $D2$) and ($D3$, $D4$), we obtain the same expressions for the flow

$$P_z = 2\cos\theta_0 + \cos p(y-x)(1+\cos^2\theta_0). \quad (29)$$

The ratio of the maximum and minimum values is

$$\eta = \frac{\min P_z}{\max P_z} = -\frac{(1-\cos\theta_0)^2}{(1+\cos\theta_0)^2}. \quad (30)$$

5.2. Three Sources

Let us see if adding a third point will improve things. Consider the triple ($D1$, $D2$, $D3$). We obtain the following expression for the energy flow

$$P_z = \cos\theta_0 + 4\cos^2 px\cos\theta_0 + 2\cos px\cos py(1+\cos^2\theta_0). \quad (31)$$

Finding the maximum value is obvious:

$$\cos px \cos py = 1 \;\Rightarrow\; \max P_z = 5\cos\theta_0 + 2(1+\cos^2\theta_0). \tag{32}$$

Finding the minimum is not at all trivial. Omitting the details, we write the final expression:

$$\min P_z = \begin{cases} -\frac{\sin^4\theta_0}{4\cos\theta_0}, & \cos\theta_0 \geq 2-\sqrt{3}, \\ 5\cos\theta_0 - 2(1+\cos^2\theta_0), & else. \end{cases} \tag{33}$$

At the transition point, continuity is maintained.

A comparison of the ratio η (minimum of P_z to its maximum) for two and three points is provided in Table 1.

Table 1. Comparison of the ratio η for two and three points located in directions at 90 degrees.

θ_0	$\theta_0 \to 0^\circ$	30°	45°	60°	$74^\circ 27'$	90°
2 points	$-{\theta_0}^4/16$	$56\sqrt{3}-97 \approx$ ≈ -0.005	$12\sqrt{2}-17 \approx$ ≈ -0.029	$-\frac{1}{9} \approx -0.111$	$-\frac{1}{3} \approx -0.333$	–1
3 points	$-{\theta_0}^4/36$	$\frac{7\sqrt{3}-15}{48\cdot 26} \approx$ ≈ -0.0023	$\frac{3\sqrt{2}-5}{56} \approx$ ≈ -0.013	$-\frac{9}{160} \approx -0.056$	$-\frac{3}{13} \approx -0.231$	–1

As can be seen from the results presented in Table 1, adding a third point impairs the value of the ratio η. It is important to note that the results of Section 4.1 do not contradict this statement, as they involve a different arrangement of points and polarizations. Other triplets consistently yield the same outcome. For the triplet ($D1$, $D3$, $D4$), the expression obtained is identical to Equation (33), and for the triplets ($D1$, $D2$, $D4$) and ($D2$, $D3$, $D4$), the same result is also achieved.

5.3. Four Sources

If we take all four points, we obtain the following expression for the flow

$$P_z = 4\cos\theta_0\left(\cos^2 px + \cos^2 py\right) + 4\cos px \cos py(1+\cos^2\theta_0). \tag{34}$$

The maximum is

$$\cos px \cos py = 1 \;\Rightarrow\; \max P_z = 8\cos\theta_0 + 4(1+\cos^2\theta_0). \tag{35}$$

This is 4 times more than for two points. Finding the minimum is more difficult, but easier than for three points. The minimum will be under the following conditions:

$$\cos px \cos py = -1 \;\Rightarrow\; \min P_z = 8\cos\theta_0 - 4(1+\cos^2\theta_0) \tag{36}$$

This is also 4 times greater than for two points. Therefore, the ratio of the minimum to the maximum η is determined by the same formula (see Equation (30)) as for two points. However, here the minimum is achieved in isolated areas (Figure 15), whereas for two points, it occurs on straight lines (Figure 1).

Thus, it has been analytically shown that even with two light points located at a 90-degree angle, with the same polarization, it is possible to form a relative reverse energy flow up to $\eta = -1$ in linear unbounded regions. It has been numerically shown that it is possible to enhance the relative reverse energy flow ($\eta < -1$) by using point sources (at least three) located at a 45-degree angle, with orthogonal polarization states. Additional enhancement is possible by introducing a second-order vortex phase singularity.

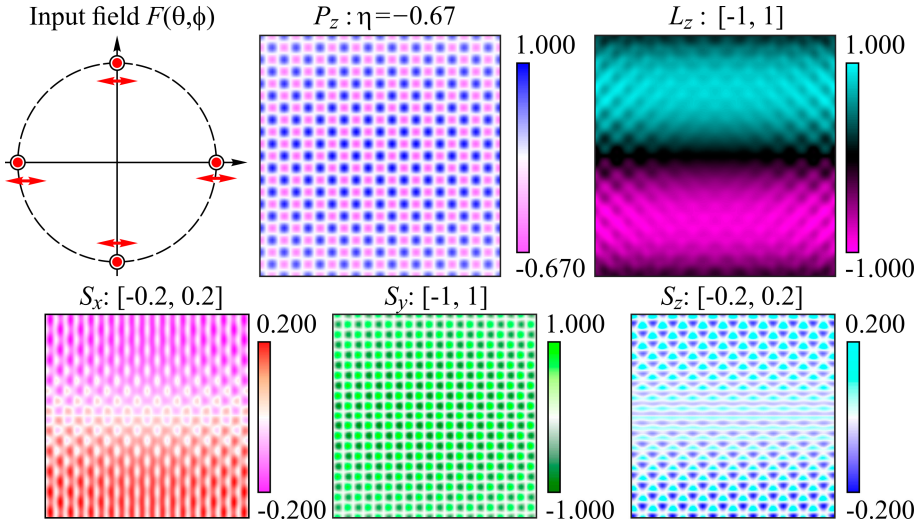

Figure 15. Results of numerical simulation for four point sources with identical linear polarizations. The labels and colors correspond to the labels and colors in Figure 1.

6. Conclusions

In this paper, we analytically and numerically investigated the possibility of forming a reverse energy flow based on the interference of radiation from a minimum number of point sources in order to obtain unbounded areas of the reverse flow. It is analytically shown that it is possible to form a reverse energy flow in linear unbounded areas using only two point sources located at an angle of 90 degrees, with the same polarization (achievable relative reverse energy flow up to $\eta = -1$).

It is shown numerically that the relative reverse energy flow can be enhanced to obtain values $\eta < -1$ by using at least three point sources located at an angle of 45 degrees with orthogonal polarization states. It is also shown numerically that additional enhancement is possible by introducing a second-order vortex phase singularity.

An important factor for the formation of the reverse flow is the asymmetric position of several point sources, i.e., at an angle of 90 or 45 degrees. The presence of an initially embedded asymmetry in the fields under consideration leads to the formation of a non-uniform distribution of SAM and OAM density. Variations in the polarization state, as well as the introduction of a vortex phase singularity, allow for changing the distribution of angular momentum density while maintaining the presence of a reverse energy flow.

In conclusion, we would like to provide some insights into potential approaches for experimentally investigating reverse energy flow. Ref. [120] demonstrates that reverse energy flow can affect electrically neutral particles with non-zero conductivity, such as ZnO particles. In this scenario, the size of these particles must be significantly smaller than the wavelength. Furthermore, in Refs. [81,90,121], we have numerically shown that a Rayleigh particle placed in the region of reverse energy flow will move in the direction opposite to that of beam propagation. Additionally, for indirect experimental evidence of reverse energy flow, the method proposed in Ref. [90] can be employed. This method relies on measuring the energy flow distribution through the intensity distribution of the light field. The observation of a very weak local maximum, known as the Arago spot, which is caused by the diffraction of the forward flow by a circle 300 nm in diameter (the diameter of the tube containing the reverse flow), has been suggested as an explanation for the existence of reverse light energy on the optical axis.

The results obtained can be used in the field of laser manipulation of nano- and microparticles. The generation of light fields with a non-uniform distribution of the angular momentum density and the Poynting vector density can affect the nature of the motion of particles trapped in different parts of such fields. The formation of such complex optical traps is also interesting due to the fact that most real nano- and micro-objects, for which one would like to use the methods of non-invasive laser manipulation,

have a non-spherical shape. These objects include various biological entities (such as spores, fungi, and cells) [122] and components of micromechanics, which are utilized in the creation of micromotors and micropumps, as well as in the optical assembly of diverse microplatforms. For instance, these microplatforms are crucial for the development of reconfigurable microenvironments for biomedical research [123,124]. Precise control of the distribution of the angular momentum of the formed optical trap will enable more accurate manipulation of such objects.

Author Contributions: Conceptualization, S.N.K. and A.V.U.; methodology, A.V.U. and S.N.K.; software, S.N.K.; validation, S.N.K., A.V.U. and A.P.P.; formal analysis, A.V.U. and S.N.K.; investigation, S.N.K., A.V.U. and A.P.P.; resources, A.V.U. and S.N.K.; data curation, S.N.K., A.V.U. and A.P.P.; writing—original draft preparation, S.N.K., A.V.U. and A.P.P.; writing—review and editing, S.N.K., A.V.U. and A.P.P.; visualization, S.N.K. and A.P.P.; supervision, S.N.K. and A.P.P.; project administration, S.N.K. and A.P.P.; funding acquisition, A.P.P. All authors have read and agreed to the published version of the manuscript.

Funding: This work was supported by the Russian Science Foundation, project no. 22-12-00041 (in part of calculation of SAM and OAM distributions), and within the State Assignment of NRC "Kurchatov Institute" (in part of theoretical analysis).

Institutional Review Board Statement: Not applicable.

Informed Consent Statement: Not applicable.

Data Availability Statement: Data underlying the results presented in this paper are not publicly available at this time but may be obtained from the authors upon reasonable request.

Conflicts of Interest: The authors declare no conflict of interests.

References

1. Andrews, D.L. *Structured Light and Its Applications: An Introduction to Phase Structured Beams and Nanoscale Optical Forces*; Academic Press: Amsterdam, The Netherlands, 2011.
2. Rubinsztein-Dunlop, H.; Forbes, A.; Berry, M.V.; Dennis, M.R.; Andrews, D.L.; Mansuripur, M.; Denz, C.; Alpmann, C.; Banzer, P.; Bauer, T. Roadmap on structured light. *J. Opt.* **2017**, *19*, 013001. [CrossRef]
3. Rosales-Guzman, C.; Ndagano, B.; Forbes, A. A review of complex vector light fields and their applications. *J. Opt.* **2018**, *20*, 123001. [CrossRef]
4. Forbes, A. Structured light from lasers. *Laser Photonics Rev.* **2019**, *13*, 1900140. [CrossRef]
5. Forbes, A.; de Oliveira, M.; Dennis, M.R. Structured light. *Nat. Photonics* **2021**, *15*, 253–262. [CrossRef]
6. Angelsky, O.V.; Bekshaev, A.Y.; Hanson, S.G.; Zenkova, C.Y.; Mokhun, I.I.; Zheng, J. Structured light: Ideas and concepts. *Front. Phys.* **2020**, *8*, 114. [CrossRef]
7. Wang, X.; Zhang, Z.; Fu, X.; Khan, A.; Zhao, S.; Gao, Y.; Jie, Y.; He, W.; Li, X.; Liu, Q.; et al. Evolution on spatial patterns of structured laser beams: From spontaneous organization to multiple transformations. *Adv. Photonics Nexus* **2023**, *2*, 024001. [CrossRef]
8. Soskin, M.S.; Vasnetsov, M.V. Singular optics. *Prog. Opt.* **2001**, *42*, 219–276. [CrossRef]
9. Gbur, G.J. *Singular Optics*; CRC Press: Boca Raton, FL, USA, 2016. [CrossRef]
10. Shen, Y.; Wang, X.; Xie, Z.; Min, C.; Fu, X.; Liu, Q.; Gong, M.; Yuan, X. Optical vortices 30 years on: OAM manipulation from topological charge to multiple singularities. *Light Sci. Appl.* **2019**, *8*, 90. [CrossRef]
11. Porfirev, A.P.; Kuchmizhak, A.A.; Gurbatov, S.O.; Juodkazis, S.; Khonina, S.N.; Kul'chin, Y.N. Phase singularities and optical vortices in photonics. *Phys. Usp.* **2022**, *192*, 841–866. [CrossRef]
12. Angelsky, O.V.; Bekshaev, A.Y.; Vasnetsov, M.V.; Zenkova, C.Y.; Maksimyak, P.P.; Jun, Z. Optical phase singularities: Physical nature, manifestations and applications. *Front. Phys.* **2022**, *10*, 1060787. [CrossRef]
13. Padgett, M.; Bowman, R. Tweezers with a twist. *Nat. Photonics* **2011**, *5*, 343–348. [CrossRef]
14. Chapin, S.C.; Germain, V.; Dufresne, E.R. Automated trapping, assembly, and sorting with holographic optical tweezers. *Opt. Express* **2006**, *14*, 13095–13100. [CrossRef] [PubMed]
15. Gómez-Viloria, I.; Nodar, Á.; Molezuelas-Ferreras, M.; Olmos-Trigo, J.; Cifuentes, Á.; Martínez, M.; Varga, M.; Molina-Terriza, G. On-axis optical trapping with vortex beams: The role of the multipolar decomposition. *ACS Photonics* **2024**, *11*, 626–633. [CrossRef] [PubMed]
16. Wang, Z.; Zhang, N.; Yuan, X.-C. High-volume optical vortex multiplexing and de-multiplexing for free-space optical communication. *Opt. Express* **2011**, *19*, 482–492. [CrossRef]
17. Wang, J.; Yang, J.-Y.; Fazal, I.M.; Ahmed, N.; Yan, Y.; Huang, H.; Ren, Y.; Yue, Y.; Dolinar, S.; Tur, M.; et al. Terabit free-space data transmission employing orbital angular momentum multiplexing. *Nat. Photonics* **2012**, *6*, 488–496. [CrossRef]

18. Khonina, S.N.; Karpeev, S.V.; Butt, M.A. Spatial-light-modulator-based multichannel data transmission by vortex beams of various orders. *Sensors* **2021**, *21*, 2988. [CrossRef]
19. Furhapter, S.; Jesacher, A.; Bernet, S.; Ritsch-Marte, M. Spiral phase contrast imaging in microscopy. *Opt. Express* **2005**, *13*, 689–694. [CrossRef]
20. Tamburini, F.; Anzolin, G.; Umbriaco, G.; Bianchini, A.; Barbieri, C. Overcoming the Rayleigh criterion limit with optical vortices. *Phys. Rev. Lett.* **2006**, *97*, 163903. [CrossRef]
21. Anand, V.; Khonina, S.; Kumar, R.; Dubey, N.; Reddy, A.N.K.; Rosen, J.; Juodkazis, S. Three-dimensional incoherent imaging using spiral rotating point spread functions created by double-helix beams. *Nanoscale Res. Lett.* **2022**, *17*, 37. [CrossRef]
22. Hnatovsky, C.; Shvedov, V.G.; Krolikowski, W.; Rode, A.V. Materials processing with a tightly focused femtosecond laser vortex pulse. *Opt. Lett.* **2010**, *35*, 3417–3419. [CrossRef]
23. Ambrosio, A.; Marrucci, L.; Borbone, F.; Roviello, A.; Maddalena, P. Light-induced spiral mass transport in azo-polymer films under vortex-beam illumination. *Nat. Commun.* **2012**, *3*, 989. [CrossRef] [PubMed]
24. Nivas, J.J.J.; Allahyari, E.; Cardano, F.; Rubano, A.; Fittipaldi, R.; Vecchione, A.; Paparo, D.; Marrucci, L.; Bruzzese, R.; Amoruso, S. Vector vortex beams generated by q-plates as a versatile route to direct fs laser surface structuring. *Appl. Surf. Sci.* **2019**, *471*, 1028–1033. [CrossRef]
25. Porfirev, A.; Khonina, S.; Kuchmizhak, A. Light–matter interaction empowered by orbital angular momentum: Control of matter at the micro-and nanoscale. *Progr. Quantum Electron.* **2023**, *88*, 100459. [CrossRef]
26. Zhan, Q. Cylindrical vector beams: From mathematical concepts to applications. *Adv. Opt. Photonics* **2009**, *1*, 1–57. [CrossRef]
27. Milione, G. Vector Beams for Fundamental Physics and Applications. Ph.D. Thesis, CUNY, New York, NY, USA, June 2016. Available online: https://academicworks.cuny.edu/gc_etds/1267 (accessed on 9 October 2024).
28. Skoulas, E.; Manousaki, A.; Fotakis, C.; Stratakis, E. Biomimetic surface structuring using cylindrical vector femtosecond laser beams. *Sci. Rep.* **2017**, *7*, 45114. [CrossRef]
29. Bautista, G.; Kakko, J.-P.; Dhaka, V.; Zang, X.; Karvonen, L.; Jiang, H.; Kauppinen, E.; Lipsanen, H.; Kauranen, M. Nonlinear microscopy using cylindrical vector beams: Applications to three-dimensional imaging of nanostructures. *Opt. Express* **2017**, *25*, 12463–12468. [CrossRef]
30. He, C.; He, H.; Chang, J.; Chen, B.; Ma, H.; Booth, M.J. Polarisation optics for biomedical and clinical applications: A review. *Light Sci. Appl.* **2021**, *10*, 194. [CrossRef]
31. Syubaev, S.A.; Zhizhchenko, A.Y.; Pavlov, D.V.; Gurbatov, S.O.; Pustovalov, E.V.; Porfirev, A.P.; Khonina, S.N.; Kulinich, S.A.; Rayappan, J.B.B.; Kudryashov, S.I.; et al. Plasmonic nanolenses produced by cylindrical vector beam printing for sensing applications. *Sci. Rep.* **2019**, *9*, 19750. [CrossRef]
32. Li, Z.X.; Ruan, Y.P.; Chen, P.; Tang, J.; Hu, W.; Xia, K.Y.; Lu, Y.Q. Liquid crystal devices for vector vortex beams manipulation and quantum information applications. *Chin. Opt. Lett.* **2021**, *19*, 112601. [CrossRef]
33. Ishitobi, H.; Nakamura, I.; Kobayashi, T.A.; Hayazawa, N.; Sekkat, Z.; Kawata, S.; Inouye, Y. Nanomovement of azo polymers induced by longitudinal fields. *ACS Photonics* **2014**, *1*, 190–197. [CrossRef]
34. Porfirev, A.P.; Khonina, S.N.; Ivliev, N.A.; Meshalkin, A.; Achimova, E.A.; Forbes, A. Writing and reading with the longitudinal component of light using carbazole-containing azopolymer thin films. *Sci. Rep.* **2022**, *12*, 3477. [CrossRef] [PubMed]
35. Porfirev, A.P.; Khonina, S.N.; Ivliev, N.A.; Porfirev, D.P.; Kazanskiy, N.L. Stacked polarizing elements for controlling parameters of surface relief gratings written in photosensitive materials. *Sensors* **2024**, *24*, 1166. [CrossRef] [PubMed]
36. Poynting, J.H. On the transfer of energy in the electromagnetic field. *Proc. R. Soc. Lond.* **1883**, *36*, 186–187. [CrossRef]
37. Allen, L.; Padgett, M.J. The Poynting vector in Laguerre–Gaussian beams and the interpretation of their angular momentum density. *Opt. Commun.* **2000**, *184*, 67–71. [CrossRef]
38. Hu, B.Y.-K. Introducing electromagnetic field momentum. *Eur. J. Phys.* **2012**, *33*, 873. [CrossRef]
39. Mörée, G.; Leijon, M. Comparison of Poynting's vector and the power flow used in electrical engineering. *AIP Adv.* **2022**, *12*, 085219. [CrossRef]
40. Simpson, N.B.; Dholakia, K.; Allen, L.; Padgett, M.J. Mechanical equivalence of spin and orbital angular momentum of light: An optical spanner. *Opt. Lett.* **1997**, *22*, 52–54. [CrossRef]
41. Stewart, A.M. Angular momentum of light. *J. Mod. Opt.* **2005**, *52*, 1145–1154. [CrossRef]
42. Yao, A.M.; Padgett, M.J. Orbital angular momentum: Origins, behavior and applications. *Adv. Opt. Photonics* **2011**, *3*, 161–204. [CrossRef]
43. Banzer, P.; Neugebauer, M.; Aiello, A.; Marquardt, C.; Lindlein, N.; Bauer, T.; Leuchs, G. The photonic wheel—Demonstration of a state of light with purely transverse angular momentum. *J. Eur. Opt. Soc.* **2013**, *8*, 6. [CrossRef]
44. Aiello, A.; Banzer, P.; Neugebauer, M.; Leuchs, G. From transverse angular momentum to photonic wheels. *Nat. Photonics* **2015**, *9*, 789–795. [CrossRef]
45. Marrucci, L.; Karimi, E.; Slussarenko, S.; Piccirillo, B.; Santamato, E.; Nagali, E.; Sciarrino, F. Spin-to-orbital conversion of the angular momentum of light and its classical and quantum applications. *J. Opt.* **2011**, *13*, 064001. [CrossRef]
46. Fleischer, A.; Kfir, O.; Diskin, T.; Sidorenko, P.; Cohen, O. Spin angular momentum and tunable polarization in high-harmonic generation. *Nat. Photonics* **2014**, *8*, 543–549. [CrossRef]
47. Devlin, R.C.; Ambrosio, A.; Rubin, N.A.; Mueller, J.P.B.; Capasso, F. Arbitrary spin-to-orbital angular momentum conversion of light. *Science* **2017**, *358*, 896–901. [CrossRef]

48. Shi, P.; Du, L.; Yuan, X. Structured spin angular momentum in highly focused cylindrical vector vortex beams for optical manipulation. *Opt. Express* **2018**, *26*, 23449–23459. [CrossRef]
49. Khonina, S.N.; Porfirev, A.P. Harnessing of inhomogeneously polarized Hermite–Gaussian vector beams to manage the 3D spin angular momentum density distribution. *Nanophotonics* **2021**, *2021 11*, 697–712. [CrossRef]
50. Albaladejo, S.; Marqués, M.I.; Laroche, M.; Sáenz, J.J. Scattering forces from the curl of the spin angular momentum of a light field. *Phys. Rev. Lett.* **2009**, *102*, 113602. [CrossRef]
51. Marqués, M.I.; Saénz, J.J. Scattering forces and electromagnetic momentum density in crossed circularly polarized standing waves. *Opt. Lett.* **2012**, *37*, 2787–2789. [CrossRef]
52. Ruffner, D.B.; Grier, D.G. Optical forces and torques in nonuniform beams of light. *Phys. Rev. Lett.* **2012**, *108*, 173602. [CrossRef]
53. Du, J.; Yuen, C.H.; Li, X.; Ding, K.; Du, G.; Lin, Z.; Chan, C.T.; Ng, J. Tailoring optical gradient force and optical scattering and absorption force. *Sci. Rep.* **2017**, *7*, 18042. [CrossRef]
54. Khonina, S.N.; Ustinov, A.V.; Volotovskiy, S.G.; Ivliev, N.A.; Podlipnov, V.V. Influence of optical forces induced by paraxial vortex Gaussian beams on the formation of a microrelief on carbazole-containing azopolymer films. *Appl. Opt.* **2020**, *59*, 9185–9194. [CrossRef] [PubMed]
55. Aiello, A.; Lindlein, N.; Marquardt, C.; Leuchs, G. Transverse angular momentum and geometric spin hall effect of light. *Phys. Rev. Lett.* **2009**, *103*, 100401. [CrossRef] [PubMed]
56. Li, M.; Yan, S.; Yao, B.; Liang, Y.; Zhang, P. Spinning and orbiting motion of particles in vortex beams with circular or radial polarizations. *Opt. Express* **2016**, *24*, 20604–20612. [CrossRef] [PubMed]
57. Emile, O.; Emile, J. Energy, linear momentum, and angular momentum of light: What do we measure? *Ann. Phys.* **2018**, *530*, 1800111. [CrossRef]
58. Pan, Y.; Gao, X.Z.; Zhang, G.L.; Li, Y.; Tu, C.; Wang, H.T. Spin angular momentum density and transverse energy flow of tightly focused kaleidoscope-structured vector optical fields featured. *APL Photonics* **2019**, *4*, 096102. [CrossRef]
59. Forbes, K.A.; Andrews, D.L. Orbital angular momentum of twisted light: Chirality and optical activity. *J. Phys. Photonics* **2021**, *3*, 022007. [CrossRef]
60. Yang, S.H.; Naaman, R.; Paltiel, Y.; Parkin, S.S.P. Chiral spintronics. *Nat. Rev. Phys.* **2021**, *3*, 328–343. [CrossRef]
61. Zhang, Z.; Mei, W.; Cheng, J.H.; Tan, Y.; Dai, Z.; Ling, X. Revisiting vortex generation in the spin-orbit interactions of refraction and focusing of light. *Phys. Rev. A* **2022**, *106*, 063520. [CrossRef]
62. Khonina, S.N.; Golub, I. Vectorial spin Hall effect of light upon tight focusing. *Opt. Lett.* **2022**, *47*, 2166–2169. [CrossRef]
63. Porfirev, A.; Khonina, S.; Ustinov, A.; Ivliev, N.; Golub, I. Vectorial spin-orbital Hall effect of light upon tight focusing and its experimental observation in azopolymer films. *Opto-Electron. Sci.* **2023**, *2*, 230014. [CrossRef]
64. Arbabi, A.; Horie, Y.; Bagheri, M.; Faraon, A. Dielectric metasurfaces for complete control of phase and polarization with subwavelength spatial resolution and high transmission. *Nat. Nanotechnol.* **2015**, *10*, 937–943. [CrossRef] [PubMed]
65. Xu, Y.; Sun, J.; Frantz, J.; Shalaev, M.I.; Walasik, W.; Pandey, A.; Myers, J.D.; Bekele, R.Y.; Tsukernik, A.; Sanghera, J.S.; et al. Reconfiguring structured light beams using nonlinear metasurfaces. *Opt. Express* **2018**, *26*, 30930–30943. [CrossRef] [PubMed]
66. Wen, D.; Crozier, K.B. Metasurfaces 2.0: Laser-integrated and with vector field control. *APL Photonics* **2021**, *6*, 080902. [CrossRef]
67. Khonina, S.N.; Butt, M.A.; Kazanskiy, N.L. A review on reconfigurable metalenses revolutionizing flat optics. *Adv. Optical Mater.* **2023**, *12*, 2302794. [CrossRef]
68. Passilly, N.; de Saint Denis, R.; Aït-Ameur, K.; Treussart, F.; Hierle, R.; Roch, J.-F. Simple interferometric technique for generation of a radially polarized light beam. *J. Opt. Soc. Am. A* **2005**, *22*, 984–991. [CrossRef]
69. Khonina, S.N.; Ustinov, A.V.; Fomchenkov, S.A.; Porfirev, A.P. Formation of hybrid higher-order cylindrical vector beams using binary multi-sector phase plates. *Sci. Rep.* **2018**, *8*, 14320. [CrossRef]
70. Gao, Y.; Chen, Z.; Ding, J.; Wang, H.-T. Single ultra-high-definition spatial light modulator enabling highly efficient generation of fully structured vector beams. *Appl. Opt.* **2019**, *58*, 6591–6596. [CrossRef]
71. Rosales-Guzmán, C.; Hu, X.-B.; Selyem, A.; Moreno-Acosta, P.; Franke-Arnold, S.; Ramos-Garcia, R.; Forbes, A. Polarisation-insensitive generation of complex vector modes from a digital micromirror device. *Sci. Rep.* **2020**, *10*, 10434. [CrossRef]
72. Baliyan, M.; Shikder, A.; Nishchal, N.K. Generation of structured light beams by dual phase modulation with a single spatial light modulator. *Phys. Scr.* **2023**, *98*, 105528. [CrossRef]
73. Yu, F.; Li, P.; Shen, H.; Mathur, S.; Lehr, C.-M.; Bakowsky, U.; Mücklich, F. Laser interference lithography as a new and efficient technique for micropatterning of biopolymer surface. *Biomaterials* **2005**, *26*, 2307–2312. [CrossRef]
74. Lai, N.D.; Liang, W.P.; Lin, J.H.; Hsu, C.C.; Lin, C.H. Fabrication of two- and three-dimensional periodic structures by multiexposure of two-beam interference technique. *Opt. Express* **2005**, *13*, 9605–9611. [CrossRef] [PubMed]
75. Vala, M.; Homola, J. Multiple beam interference lithography: A tool for rapid fabrication of plasmonic arrays of arbitrary shaped nanomotifs. *Opt. Express* **2016**, *24*, 15656–15665. [CrossRef] [PubMed]
76. Rebollar, E.; Castillejo, M.; Ezquerra, T.A. Laser induced periodic surface structures on polymer films: From fundamentals to applications. *Eur. Polym. J.* **2015**, *73*, 162–174. [CrossRef]
77. Uesugi, Y.; Miwa, T.; Kadoguchi, N.; Kozawa, Y.; Sato, S. Multi-beam ultrafast laser processing of free-standing nanofilms. *Appl. Phys. A* **2023**, *129*, 101. [CrossRef]
78. Khonina, S.N.; Ustinov, A.V.; Porfirev, A.P.; Karpeev, S.V. Analysis of the polarization distribution and spin angular momentum of the interference field obtained by co-planar beams with linear and circular polarization. *Photonics* **2024**, *11*, 478. [CrossRef]

79. Vaveliuk, P.; Martinez-Matos, O. Negative propagation effect in nonparaxial Airy beams. *Opt. Express* **2012**, *20*, 26913–26921. [CrossRef]
80. Novitsky, A.; Qiu, C.-W.; Wang, H. Single gradientless light beam drags particles as tractor beams. *Phys. Rev. Lett.* **2011**, *107*, 203601. [CrossRef]
81. Nalimov, A.G.; Stafeev, S.S.; Kotlyar, V.V. Optical force acting on a particle in a reverse energy flow near the focus of a gradient lens. *J. Opt.* **2020**, *22*, 115001. [CrossRef]
82. Kotlyar, V.V.; Nalimov, A.G.; Kovalev, A.A.; Porfirev, A.P. Experimental investigation of the energy backflow in the tight focal spot. *Comput. Opt.* **2020**, *44*, 864–871. [CrossRef]
83. Kotlyar, V.V.; Stafeev, S.S.; Nalimov, A.G. Energy backflow in the focus of a light beam with phase or polarization singularity. *Phys. Rev. A* **2019**, *99*, 033840. [CrossRef]
84. Khonina, S.N.; Ustinov, A.V.; Degtyarev, S.A. Inverse energy flux of focused radially polarized optical beams. *Phys. Rev. A* **2018**, *98*, 043823. [CrossRef]
85. Li, H.; Wang, C.; Tang, M.; Li, X. Controlled negative energy flow in the focus of a radial polarized optical beam. *Opt. Express* **2020**, *28*, 18607–18615. [CrossRef] [PubMed]
86. Khonina, S.N.; Ustinov, A.V. Increased reverse energy flux area when focusing a linearly polarized annular beam with binary plates. *Opt. Lett.* **2019**, *44*, 2008–2011. [CrossRef] [PubMed]
87. Stafeev, S.S.; Kotlyar, V.V. Elongation of the area of energy backflow through the use of ring apertures. *Opt. Commun.* **2019**, *450*, 67–71. [CrossRef]
88. Ustinov, A.V.; Khonina, S.N.; Porfirev, A.P. Formation of inverse energy flux in the case of diffraction of linearly polarized radiation by conventional and generalized spiral phase plates. *Photonics* **2021**, *8*, 283. [CrossRef]
89. Khonina, S.N.; Porfirev, A.P.; Ustinov, A.V.; Kirilenko, M.S.; Kazanskiy, N.L. Tailoring of inverse energy flow profiles with vector Lissajous beams. *Photonics* **2022**, *9*, 121. [CrossRef]
90. Kotlyar, V.V.; Stafeev, S.S.; Nalimov, A.G.; Kovalev, A.A.; Porfirev, A.P. Mechanism of formation of an inverse energy flow in a sharp focus. *Phys. Rev. A* **2020**, *101*, 033811. [CrossRef]
91. Saari, P.; Besieris, I. Backward energy flow in simple four-wave electromagnetic fields. *Eur. J. Phys.* **2021**, *42*, 055301. [CrossRef]
92. Khonina, S.N.; Golub, I. Breaking the symmetry to structure light. *Opt. Lett.* **2021**, *46*, 2605–2608. [CrossRef]
93. Mansuripur, M. Certain computational aspects of vector diffraction problems. *J. Opt. Soc. Am. A* **1989**, *6*, 786–805. [CrossRef]
94. Guo, H.; Chen, J.; Zhuang, S. Vector plane wave spectrum of an arbitrary polarized electromagnetic wave. *Opt. Express* **2006**, *14*, 2095–2100. [CrossRef] [PubMed]
95. Ciattoni, A.; Crosignani, B.; Porto, P.D. Vectorial analytical description of propagation of a highly non paraxial beam. *Opt. Commun.* **2002**, *202*, 17–20. [CrossRef]
96. Li, J.; Zhu, S.; Lu, B. The rigorous electromagnetic theory of the diffraction of vector beams by a circular aperture. *Opt. Commun.* **2009**, *282*, 4475–4480. [CrossRef]
97. Khonina, S.N.; Kharitonov, S.I. An analog of the Rayleigh–Sommerfeld integral for anisotropic and gyrotropic media. *J. Mod. Opt.* **2013**, *60*, 814–822. [CrossRef]
98. Khonina, S.N.; Ustinov, A.V.; Kovalyov, A.A.; Volotovsky, S.G. Near-field propagation of vortex beams: Models and computation algorithms. *Opt. Mem. Neural Netw.* **2014**, *23*, 50–73. [CrossRef]
99. Richards, B.; Wolf, E. Electromagnetic diffraction in optical systems, II. Structure of the image field in an aplanatic system. *Proc. R. Soc. Lond. Ser. A Math. Phys. Sci.* **1959**, *253*, 358–379. [CrossRef]
100. Helseth, L.E. Optical Vortices in Focal Regions. *Opt. Commun.* **2004**, *229*, 85–91. [CrossRef]
101. Wu, G.; Lou, Q.; Zhou, J. Analytical vectorial structure of hollow Gaussian beams in the far field. *Opt. Express* **2008**, *16*, 6417–6424. [CrossRef]
102. Zhou, G. The analytical vectorial structure of a nonparaxial Gaussian beam close to the source. *Opt. Express* **2008**, *16*, 3504–3514. [CrossRef]
103. Volyar, A.V.; Shvedov, V.G.; Fadeeva, T.A. The Structure of a Nonparaxial Gaussian Beam near the Focus: II. Optical Vortices. *Opt. Spectrosc.* **2001**, *90*, 93–100. [CrossRef]
104. Mitri, F.G. Superposition of nonparaxial vectorial complex-source spherically focused beams: Axial Poynting singularity and reverse propagation. *Phys. Rev. A* **2016**, *94*, 023801. [CrossRef]
105. Felsen, L.B. Complex-Source-Point-Solutions of the Field Equations and Their Relation to the Propagation and Scattering of Gaussian Beams. In *Symposia Matematica, Instituto Nazionale di Alta Matematica XVIII*; Academic Press: London, UK, 1976; pp. 39–56.
106. Norris, A.N. Complex point-source representation of real point sources and the Gaussian beam summation method. *J. Opt. Soc. Am. A* **1986**, *3*, 2005–2010. [CrossRef]
107. Bekshaev, A.Y.; Bliokh, K.Y.; Nori, F. Transverse spin and momentum in two-wave interference. *Phys. Rev. X* **2015**, *5*, 011039. [CrossRef]
108. Xu, X.; Nieto-Vesperinas, M. Azimuthal imaginary Poynting momentum density. *Phys. Rev. Lett.* **2019**, *123*, 233902. [CrossRef]
109. Khonina, S.N.; Degtyarev, S.A.; Ustinov, A.V.; Porfirev, A.P. Metalenses for the generation of vector Lissajous beams with a complex Poynting vector density. *Opt. Express* **2021**, *29*, 18651–18662. [CrossRef]

110. Bekshaev, A. Dynamical characteristics of electromagnetic field under conditions of total internal reflection. *J. Opt.* **2018**, *20*, 045604. [CrossRef]
111. Holbourn, A. Angular momentum of circularly polarised light. *Nature* **1936**, *137*, 31. [CrossRef]
112. Garcés-Chávez, V.; McGloin, D.; Padgett, M.J.; Dultz, W.; Schmitzer, H.; Dholakia, K. Observation of the transfer of the local angular momentum density of a multiringed light beam to an optically trapped particle. *Phys. Rev. Lett.* **2003**, *91*, 093602. [CrossRef]
113. Zhang, Y.; Xue, Y.; Zhu, Z.; Rui, G.; Cui, Y.; Gu, B. Theoretical investigation on asymmetrical spinning and orbiting motions of particles in a tightly focused power-exponent azimuthal-variant vector field. *Opt. Express* **2018**, *26*, 4318–4329. [CrossRef]
114. Bliokh, K.Y.; Nori, F. Transverse spin of a surface polariton. *Phys. Rev. A* **2012**, *85*, 061801. [CrossRef]
115. Bliokh, K.Y.; Nori, F. Transverse and longitudinal angular momenta of light. *Phys. Rep.* **2015**, *592*, 1–38. [CrossRef]
116. Khonina, S.N.; Ustinov, A.V.; Porfirev, A.P. Vector Lissajous laser beams. *Opt. Lett.* **2020**, *45*, 4112–4115. [CrossRef] [PubMed]
117. Bliokh, K.Y.; Alonso, M.A.; Ostrovskaya, E.A.; Aiello, A. Angular momenta and spin-orbit interaction of nonparaxial light in freespace. *Phys. Rev. A* **2010**, *82*, 063825. [CrossRef]
118. Zhu, W.G.; She, W.L. Transverse angular momentum and transverse barycenter shift of a focused light field due to nonuniform input angular momentum. *Opt. Lett.* **2014**, *39*, 1337–1340. [CrossRef]
119. Beijersbergen, M.W.; Coerwinkel, R.P.C.; Kristensen, M.; Woerdman, J.P. Helical-wave-front laser-beams produced with a spiral phase plate. *Opt. Commun.* **1994**, *112*, 321–327. [CrossRef]
120. Berry, M.V. Optical currents. *J. Opt. A-Pure Appl. Opt.* **2009**, *11*, 094001. [CrossRef]
121. Kotlyar, V.V.; Stafeev, S.S.; Nalimov, A.G.; Kovalev, A.A. Formation of the reverse flow of energy in a sharp focus. *Comput. Opt.* **2019**, *43*, 714–722. [CrossRef]
122. Barber, P.W. Scattering and absorption efficiencies for nonspherical dielectric objects-biological models. *IEEE Trans. Biomed. Eng.* **1978**, *BME-25*, 155–159. [CrossRef]
123. Maruo, S.; Takaura, A.; Saito, Y. Optically driven micropump with a twin spiral microrotor. *Opt. Express* **2009**, *17*, 18525–18532. [CrossRef]
124. Rodrigo, P.J.; Kelemen, L.; Palima, D.; Alonzo, C.A.; Ormos, P.; Glückstad, J. Optical microassembly platform for constructing reconfigurable microenvironments for biomedical studies. *Opt. Express* **2009**, *17*, 6578–6583. [CrossRef]